

CORRELATION OF He II LYMAN ALPHA WITH He I 10830 Å, AND WITH CHROMOSPHERIC AND EUV CORONAL EMISSION

W. T. THOMPSON

Applied Research Corporation, 8201 Corporate Drive, Landover, MD 20785, U.S.A.

W. M. NEUPERT, S. D. JORDAN

*NASA Goddard Space Flight Center, Laboratory for Astronomy and Solar Physics, Code 680,
Greenbelt, MD 20771, U.S.A.*

H. JONES, R. J. THOMAS

*NASA Goddard Space Flight Center, Laboratory for Astronomy and Solar Physics, Code 682,
Greenbelt, MD 20771, U.S.A.*

and

B. SCHMIEDER

Observatoire de Paris, Section Meudon, UA 326, F-92195 Meudon Principal Cedex, France

(Received 2 November, 1992; in revised form 26 January, 1993)

Abstract. This paper describes the results of comparing SERTS-3 images obtained in the transition region line of He II 304 Å with chromospheric He I 10830 Å absorption, with strong coronal lines of Mg IX 368 Å, Fe XV 284 Å and 417 Å, and Fe XVI 335 Å and 31 Å, with H α , with Ca II 8542 Å, and with magnetograms in Fe I 8688H α . All of the images are illustrated, and the image reconstruction techniques used are described and evaluated. The high correlation of the He II 304 Å and He I 10830 Å images, originally found by Harvey and Sheeley (1977), is confirmed and is put on a quantitative basis. We find that the supergranulation network has greater contrast, and that filaments appear darker, in 10830 Å than in 304 Å. In active regions, the 304 Å line follows more closely the behavior of H α and Ca II 8542 Å than the 10830 Å line.

1. Introduction

The formation mechanisms for the He II 304 Å line and the He I 10830 Å line in different solar features, as well as the contribution of the 304 Å line to the transition region energy balance and the coronal energy balance itself, are all important problems in solar physics that have so far evaded complete solution. In view of the comparatively small spatial scale on which many of the features in question occur, data of high spatial resolution on the scale of a few arc sec are needed to perform a meaningful analysis. Finally, if coregistered images in the He I 10830 Å line can be obtained together with the transition region and coronal observations, the roles of both the coronal radiation and the 304 Å line in the formation of 10830 Å can be assessed.

Such a data set was obtained on May 5, 1989, during and in association with the third flight of the Goddard Solar EUV Rocket Telescope and Spectrograph (SERTS-3). A description of the instrument and its 1989 observations appear in Neupert *et al.* (1992b). Here we present the results of image processing on these

data. The calibrated spectra and some results on coronal velocities are described elsewhere (Thomas and Neupert, 1993; Neupert *et al.*, 1992a). An analysis of the He II 304 Å formation mechanism based on these data appears in Jordan *et al.* (1993).

In this paper, we describe the image reconstruction techniques used to deconvolve the point spread function of the SERTS instrument from the observations, and evaluate their effectiveness. The resulting reconstructed He II 304 Å images are then compared with coregistered He I 10830 Å images. The high correlation previously observed by Harvey and Sheeley (1977) between these two wavelengths is confirmed, with areas of exception described and noted. The 304 Å images are also compared with coordinated observations made of H α intensity and velocity, with strong coronal lines from SERTS-3, with Ca II, and with a photospheric magnetogram.

The correlations between He I and He II are put on a qualitative basis, and the deviations from the average behaviour are described and analyzed. The results are compared to the qualitative observations of Harvey and Sheeley (1977). The effects of image reconstruction on the quantitative results are examined.

2. Brief Description of the Instrument

The Solar EUV Rocket Telescope and Spectrograph (SERTS) is a sounding rocket experiment designed to obtain spatially resolved high resolution spectra, and non-overlapping spectroheliograms over a wide range of extreme ultraviolet (EUV) wavelengths characteristic of temperatures between 5×10^4 – 3×10^7 K. SERTS uses a Wolter Type-2 grazing incidence telescope to focus an image of the Sun onto the entrance aperture of a normal incidence spectrograph. A detailed description of the instrument can be found in Neupert *et al.* (1992b).

The entrance aperture assembly uses a unique 'hourglass' design to simultaneously obtain spectroheliogram images and high resolution spectra (see Figure 1). The top and bottom parts of the aperture each cover a large area of the Sun, approximately 5×8 arc min each. These regions are seen at the detector as spectroheliogram images in each of the strong spectral lines. In between these two lobes is a narrow slit portion ~ 5 arc min long and only 1.5 arc sec wide, which gives us high resolution spectra. After taking exposures at one position on the Sun, the pointing is changed so that the narrow slit portion of the aperture covers an area formerly covered by one of the broad lobes, and the other lobe covers the area formerly covered by the slit. That way we obtain near simultaneous spectroheliograms images and highly resolved spectra of the same areas on the Sun.

The spectrograph employs a normal incidence toroidal grating with stigmatically refocuses spectral images of the aperture between 235–450 Å onto the film plane. Kodak EK 101-07 film is used to record the data.

The result spatial resolution of the instrument approaches 5 arc sec, which is comparable to that obtained by Skylab observations at 304 Å from the S055 (HCO)

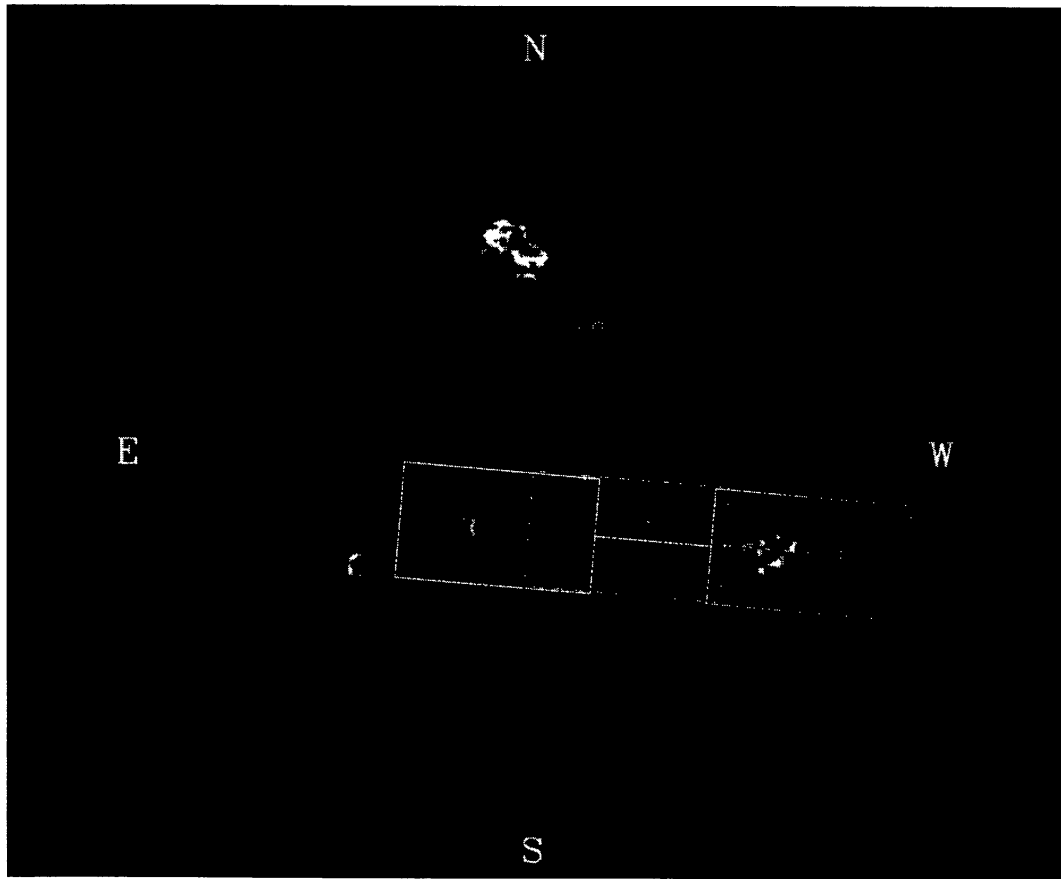


Fig. 1. H α image from Big Bear Solar Observatory taken on the day of the SERTS flight, showing the configuration and position of the SERTS aperture during the exposures. The solid outline shows the approximate pointing of the SERTS instrument for the first pointing position (frames 1 and 2). The dashed outline shows the approximate pointing for the second pointing position (frame 3).

and S082A (NRL) experiments. In addition, SERTS has much better spectral resolution and sensitivity at 304 Å than S055 provided, and does not suffer from nearly as much spectral overlapping as characterized the S082A images.

3. SERTS Spectroheliograms and Enhancement Techniques

During the flight of May 5, 1989, spectroheliograms and spectra were obtained for an active region (AR 5464) near the west limb of the Sun. Figure 1 shows a Big Bear solar image from the day of the SERTS-3 flight. The first two SERTS exposures, of 97 and 20 s each, were taken with the active region located in one of the two lobes, as shown in Figure 1. The other lobe was located approximately due east nearer the center of the Sun. The second SERTS pointing position, with the slit cutting through the active region, was exposed for a total of 246 s in one exposure. Table I shows the times of each SERTS exposure, and of the coordinated observations used in this report.

Figure 2 shows spectroheliogram images from the SERTS-3 flight in a number

TABLE I
Times in UT of each SERTS-3 exposure
(mid-point), and of the ground-based observations

Observation	Time (UT)	Duration (s)
SERTS-3, No. 1	17:47:30.5	97.4
SERTS-3, No. 2	17:48:30.5	20.4
SERTS-3, No. 3	17:50:54.4	246.3
Fe 8688 (mag)	13:37:10	–
He 10830 (FD)	14:31:07	–
H α	17:43:54	–
He 10830 (AR)	17:57	–
Ca 8542	18:30	–

Note: FD=full disk; AR=active region.

of spectral lines. The images in the left and right columns are from the east and west lobes respectively during the first two exposures. The most suitable exposure was used for each image. The middle column is from the third exposure, and covers the area of the Sun between the other two. There is an approximately 30% overlap between the images in the left and middle columns, and a small area of overlap between the middle and right column images. The greyscale has been adjusted for each image so that the maximum dynamic range can be displayed – the differences in intensities between the lines are not reflected (see Thomas and Neupert (1993) for a list of absolute line intensities observed during the SERTS-3 flight).

3.1. FILM CALIBRATION

The SERTS-3 images were digitized using a Perkin–Elmer 1010M microdensitometer with a $10 \times 10 \mu\text{m}$ aperture, corresponding to ~ 0.9 arc sec resolution. The characteristic curve of the film was obtained from a pixel-by-pixel comparison of the first two exposures (averaged to $100 \times 100 \mu\text{m}$ resolution) which shared the same solar pointing.

The characteristic curve was fitted to the function

$$\log_{10} E = \begin{cases} A_0 + A_1 \log_{10}(10^{A_2 D} - 1), & \text{for } D \leq A_4, \\ A_0 + A_1 \log_{10}(10^{A_2 D} - 1) + A_3(D - A_4)^2, & \text{for } D > A_4, \end{cases}$$

so that the log of the ratio of E inferred from the second exposure to that inferred from the first was a constant based on the exposure times. (The parameter A_0 was not fitted.) This is similar to functions used by other researchers (Tsubaki and Engvold, 1975; Lehmann and Häupl, 1986; Cook, Ewing, and Sutton, 1988), but modified to take into account the fact that the Kodak EK 101–107 film saturates at a lower density when exposed to EUV radiation than it does for visible light.

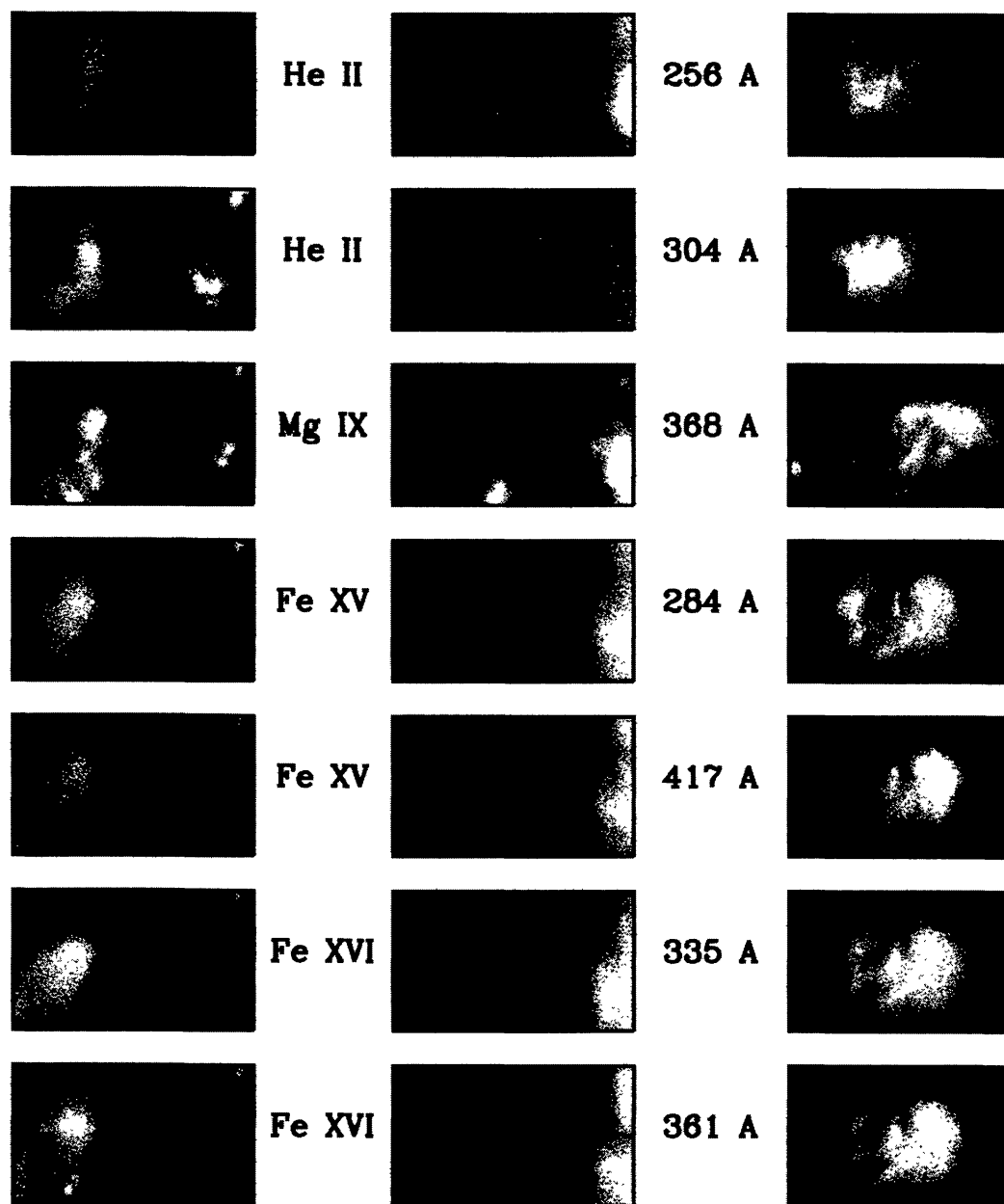


Fig. 2. SERTS spectroheliogram images in a number of spectral lines. The left and right columns are from the east and west lobes during the first two exposures. The middle column is from the third exposure, and covers the area of the Sun between the other two. There is $\sim 30\%$ overlap between the left and middle images and a small area of overlap between the middle and right images.

The overlap region from the third exposure was then coregistered to the first two, and was used as a check on the correctness of the derived curve. An attempt was made to account for changes in the atmospheric extinction between the different exposures, but the most consistent results were obtained by assuming that the extinction was constant over the flight.

For SERTS-3 a separate characteristic curve was derived for three different wavelength regions, and then interpolated to form a continuous function. Since then we have simplified the procedure to fit a single characteristic curve for all

the observed wavelengths, since no consistent wavelength effect could be demonstrated.

Photometric calibrations were performed for each of the optical components carried on the 1989 and 1991 flights of this experiment, either in our GSFC EUV evaluation lab or at the NIST SURF-II synchrotron facility. Calculations were also made of the atmospheric EUV extinction at rocket altitudes for each flight, resulting in a relative intensity scale good to $\pm 25\%$ over the first-order spectral range. This was checked by comparing observed solar ratios of density-insensitive line pairs against their theoretically known values. An absolute photometric scale accurate to within a factor of 2 was then derived by fitting our solar observations to reported values for the average He II quiet-Sun flux at 304 Å.

3.2. IMAGE RECONSTRUCTION

The characteristics of the grazing-incidence SERTS-A telescope used in the SERTS-3 flight are such that although the core of the point spread function is less than 5 arc sec in width, much of the energy in the image is actually spread out in broad wings about the central core. Figure 3 shows the point- and line-spread functions of the SERTS-A telescope. (The SERTS-3 images were not appreciably affected by rocket motions, since pointing stability was better than 1 arc sec except for one unplanned step of 2.6 arc sec during the first exposure.)

To remove the telescope point-spread function from the SERTS images, we applied two different deconvolution strategies: Fourier deconvolution (Brault and White, 1971) and Richardson–Lucy (Lucy, 1974) deconvolution. Other deconvolution strategies are being studied for astronomical applications, but these two are the simplest to implement. Since our point-spread function was assumed to be constant over the image, and we did not try to bound the solutions in any way, other image reconstruction techniques should give similar results.

Figure 4 shows the effects of image deconvolution on the He II images. It was found that unless some care was taken with the filter function used in the Fourier technique, then the reconstructed image took on a ‘pebbly’ appearance. This is due to the amplification of granular structures within the film, and to the depression of high-frequency amplitudes. The filtering used is based on Brault and White (1971), who show that the optimal filter function can be expressed as

$$\Phi(\nu) = \frac{P_S(\nu)}{P_S(\nu) + P_N(\nu)},$$

where P_S is the power spectrum of the smeared image in the absence of noise, and P_N is the power spectrum of the noise. Of course, these quantities cannot be determined directly from the image. However, for most applications it is only necessary that a good approximation be made. We estimated P_S by the power spectrum of the point-spread function, with the philosophy that the image power is unlikely to exceed this, and P_N by a constant. This approach was taken to minimize

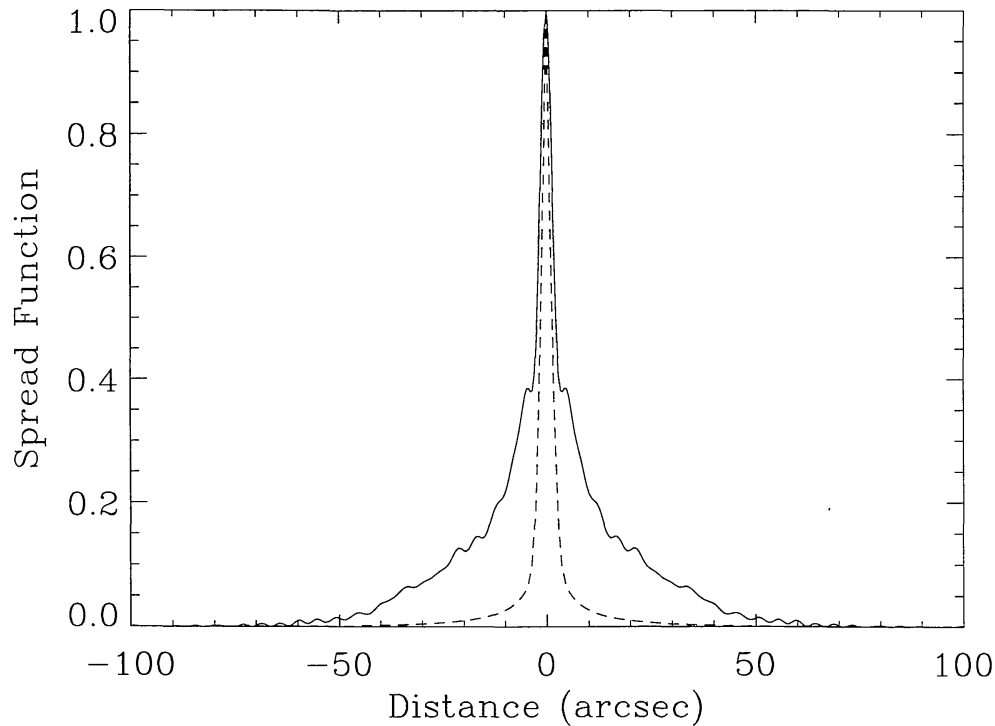


Fig. 3. Solid line shows the line spread function of the SERTS-A telescope at 304 Å as measured in the laboratory. The dashed line shows the point-spread function inferred from the line-spread function. The imaging properties of the central core of the line- and point-spread functions are determined mainly by the accuracy of the overall shape and alignment of the optical components of the telescope. The broad wings are due to mid- and high-frequency surface errors on the optical surfaces.

the possibility of overfiltering. We also tried combining this with a Gaussian high-frequency rolloff, but this was found to emphasize the film grains. The value of P_N also affected the amplification of film grain, although no value could be found which made the effect go away completely.

The Richardson–Lucy technique has a different frequency response than the Fourier technique – most of the correction is applied at those frequencies where the point-spread function has more energy. The image in Figure 4 was generated by starting the iterative process with a smoothed version of the original unreconstructed image. However, we also did tests where the iteration began with an unsmoothed image. The difference in the way the Fourier and Richardson–Lucy techniques handle the high-frequency noise was explored by examining the power spectra of the original and reconstructed images. The filter function used in the Fourier technique depresses the power at high frequencies – otherwise they would be over-reconstructed when the image was reconstructed. With the Richardson–Lucy technique, the amount of power at high frequencies was basically unaffected. Thus, the reconstructed image has no more noise than the unreconstructed image, even when the first iteration was the original image.

Comparing the two sets of reconstructed images in Figure 4, it can be seen that small-scale features look somewhat sharper in the images produced with

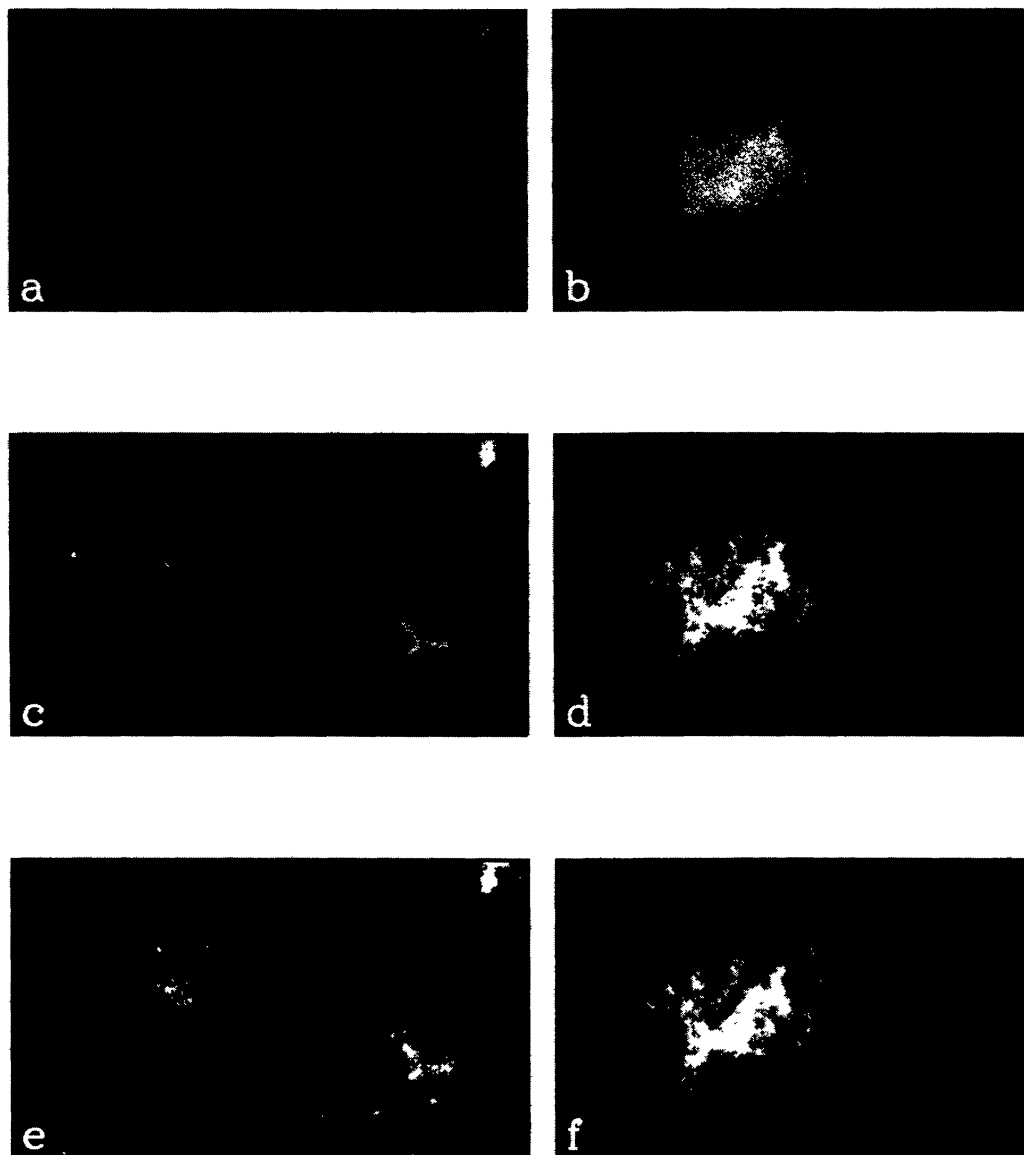


Fig. 4. Effect of image deconvolution on the He 304 Å images. (a) and (b) are the original 304 Å images of the SERTS-3 east and west lobes, respectively. (c) and (d) have been processed using Fourier deconvolution, and (e) and (f) with Richardson-Lucy deconvolution.

the Richardson-Lucy technique. This is most likely because of the loss of high-frequency information in the Fourier technique.

The image restoration process appears to work mostly by recovering the light distributed in the broad wings of the point-spread function, where most of the energy is. There does not appear to be any sharpening of the central core. The situation may change when these reconstruction techniques are applied to the images taken during the SERTS-4 flight (Davila *et al.*, 1992). The improved telescope used on that flight put much more energy into the central core (Leviton *et al.*, 1993).

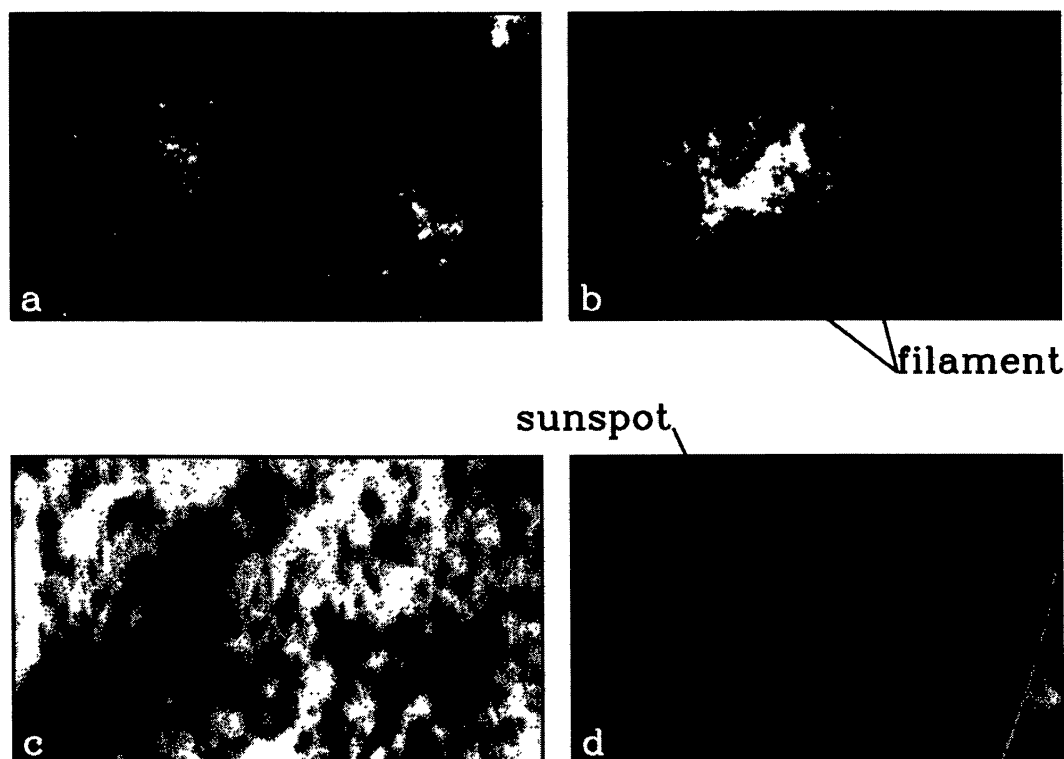


Fig. 5. Comparison of He II 304 Å, ((a) east lobe, (b) west lobe) to corresponding He I 10830 Å ((c) and (d)) from the National Solar Observatory in Kitt Peak, Arizona. The indicated sunspot appears as a blank area of data dropout in the 10830 Å image.

4. Comparison of SERTS Images with Other Observations

4.1. COMPARISON OF He I AND He II IMAGES

Coordinated He I 10830 Å observations were made at the National Solar Observatory* at Kitt Peak Arizona. Figure 5 shows the comparison between the He II 304 Å image from SERTS-3 and He I 10830 Å. These images were coaligned by selecting features that appeared the same in both images, and making least-squares fits to determine the position, orientation, and scale. This was judged to yield a coalignment accurate to within ± 5 arc sec. In the following analysis the full disk He I 10830 Å image taken before the SERTS-3 flight was used, so that both quiet Sun and active region areas could be studied. The smaller active region image taken just after the flight (Table I) was compared with the earlier image to verify that no significant changes occurred over that time frame.

Examining Figure 5 shows that features in emission in He II appear to be highly correlated with features in absorption in He I. Filaments represent an exception to this rule, in that they are dark in both He I, and (generally) in He II, although less so in He II. Bright plage material often appears in conjunction with the filament

* The National Solar Observatory is a Division of the National Optical Astronomy Observatories which is operated by the Association of Universities for Research in Astronomy, Inc., under cooperative agreement with the National Science Foundation.

in He II – a good example of this is the large filament extending across the active region in the west lobe. Another exception is the bright plage material surrounding the sunspot in the west lobe, which does not seem to have an exact counterpart in the He I image. No value for the He I 10830 Å equivalent width could be obtained within the sunspot itself, so that it appears as a blank spot in the 10830 Å image.

4.2. COMPARISON WITH OTHER SPECIES

Coordinated observations were taken at ground-based observatories in H α , in the Ca II 8542 Å line, and in the Fe I 8688 Å line in which magnetograms were obtained. Coregistered images in these lines and in the He 304 Å and 10830 Å lines add to the value of the SERTS-3 data set by permitting a comparison with other indicators of photospheric and chromospheric structure, and with potential field calculations based on the Fe 8688 Å magnetograms (Neupert *et al.*, 1992a). All these images were coaligned in the same manner as He I 10830 Å (Section 4.1).

A comparison of the SERTS-3 images of the active region in 304 Å with an H α image obtained with the Multichannel Subtractive Double Pass (MSDP) Spectrograph operating at the Solar Tower at Meudon appears in Figure 6. The MSDP technique allows the reconstruction of the H α line profile at each point of the solar field of view, and the derivation of intensity and Dopplershift maps (Mein and Mein, 1977). One sees that much of the plage material visible in H α can also be seen in 304 Å. In particular, the bright plages below and to the right of the sunspot appear to be highly correlated with similar features in 304 Å, but not with 10830 Å. This suggests that the mechanism heating the plage differs from that responsible for producing the ground state of 10830 Å, at least in part.

Figure 6(c) is a velocity image derived from the H α data. The regions of strong He II 304 Å emission are also regions of strong H α velocity, with both positive and negative velocities appearing. However, one cannot make a strong correlation between the 304 Å intensity values and the magnitude of the H α velocity.

The He II 304 Å radiation can also be said to be correlated with the coronal EUV emission (Figure 2), particularly in the quiet-Sun areas. However, again this correlation breaks down in the brightest plage areas surrounding the sunspot, also implying that a different mechanism controls the 304 Å line in this region.

A further comparison between 304 Å and chromospheric conditions, as seen in the Ca II 8542 Å line, is provided in Figure 7. This image was derived from one of the first spectra-spectroheliograms ever obtained with the NASA/NSO Spectromagnetograph (Jones *et al.*, 1992) at Kitt Peak. Here the overall correspondence may be the best of all the comparisons made here. Since Avrett (1985) identifies the 8542 Å line as involved in strong cooling of the chromosphere, this suggests that the local heating mechanisms that balance the cooling in the two lines, one chromospheric and one transition region, may be closely related, even if differing in detail as suggested by Anderson and Athay (1989).

Also, Figure 8 shows the relationship between the He II 304 Å intensity with structures in the magnetic field, using an NSO (Kitt Peak) magnetogram taken in

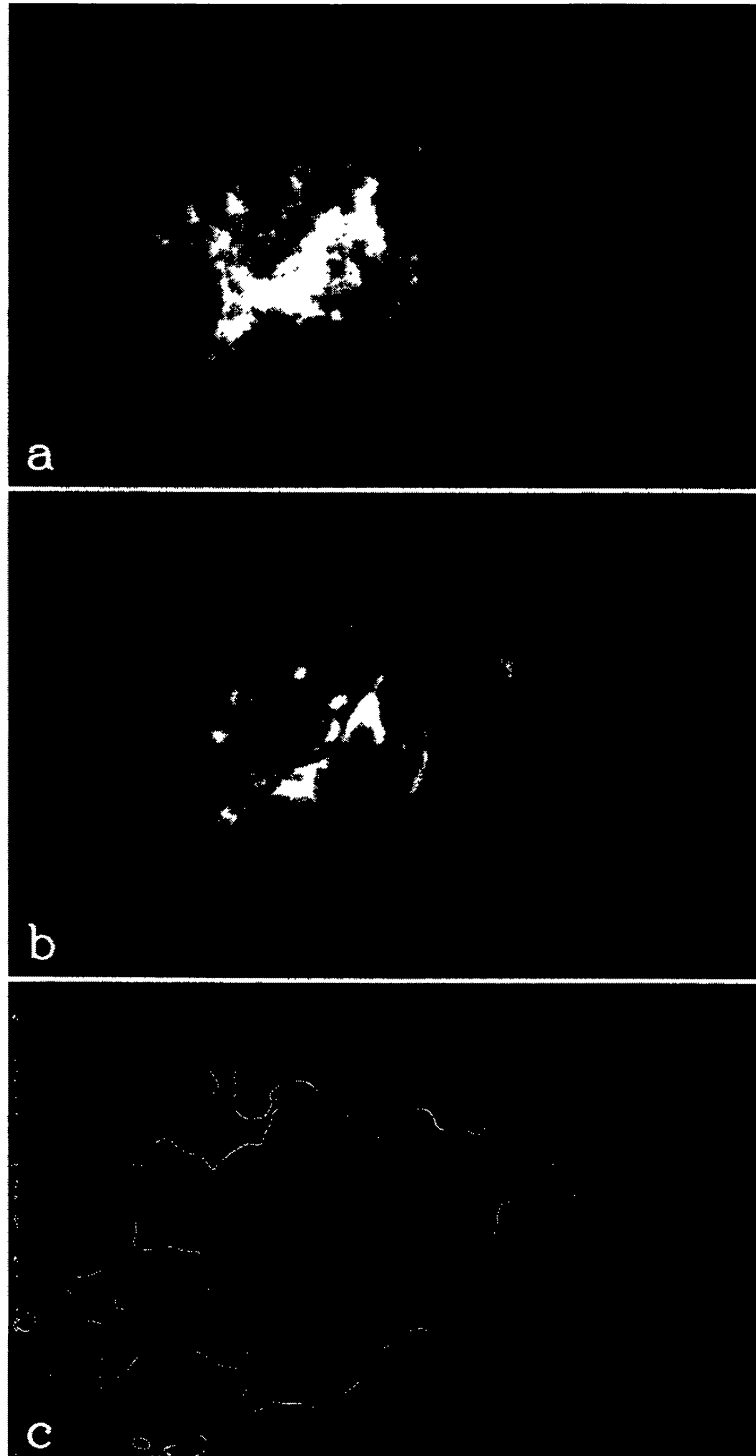


Fig. 6. Comparison of the He II 304 Å image of the active region (a) to a simultaneous and coregistered Hα image (b) obtained with the MSDP at the Solar Tower in Meudon, France. Also shown is a velocity image derived from the Hα data (c), where white areas represent motion toward the observer, and dark areas represent motion away from the observer. An isocontour representing strong 304 Å emission is overlaid on the velocity image.

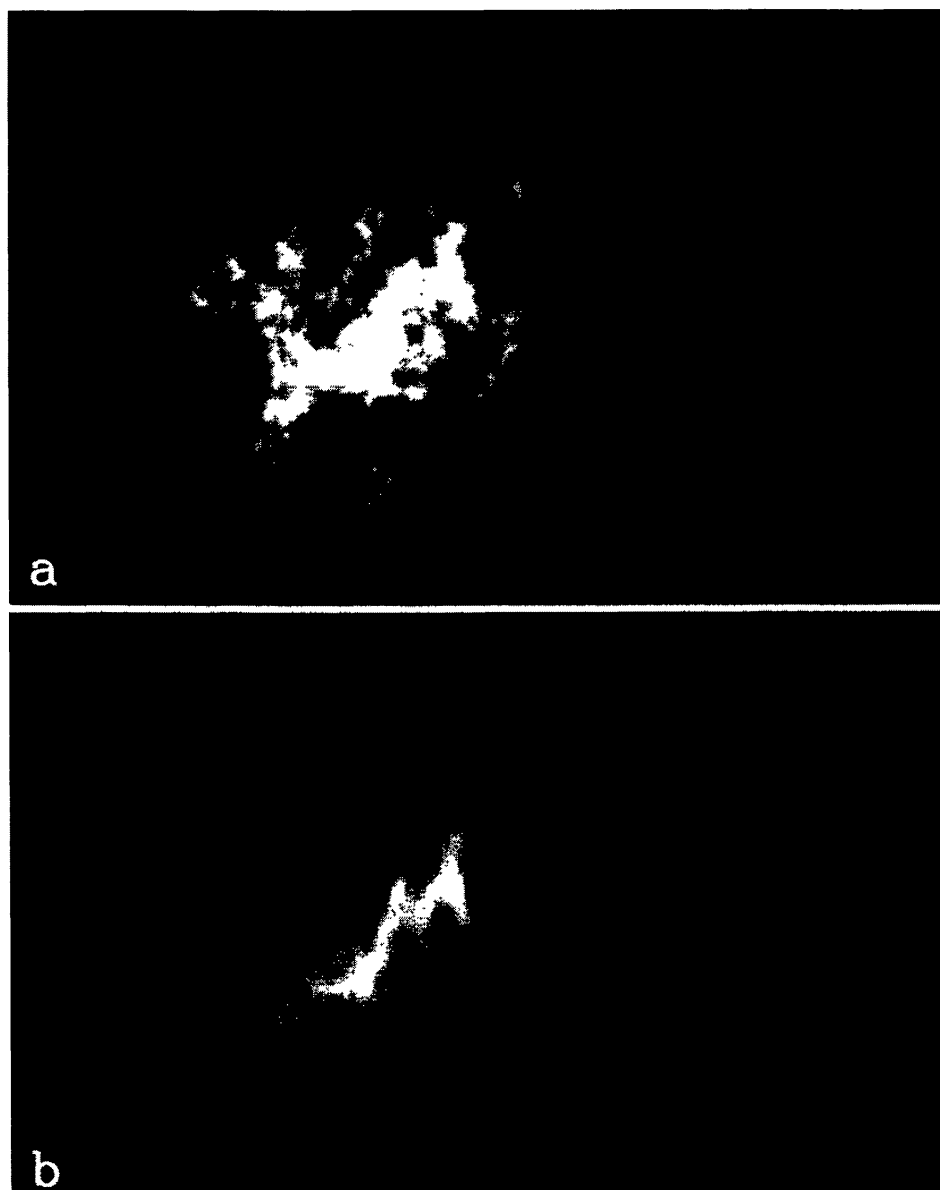


Fig. 7. Comparison of the He II 304 Å image of the active region (a) to a coregistered Ca II 8542 Å image from the National Solar Observatory at Kitt Peak, Arizona (b).

Fe I 8688 Å. The relationship between He II emission and strong magnetic structures is quite evident. These magnetograms and potential field calculations based upon them permitted Neupert *et al.* (1992a) to conclude that the site of the source of material upflow observed in the Mg IX 368 Å line with SERTS-3 was consistent with origins of low-speed solar wind inferred from interplanetary plasma observations.

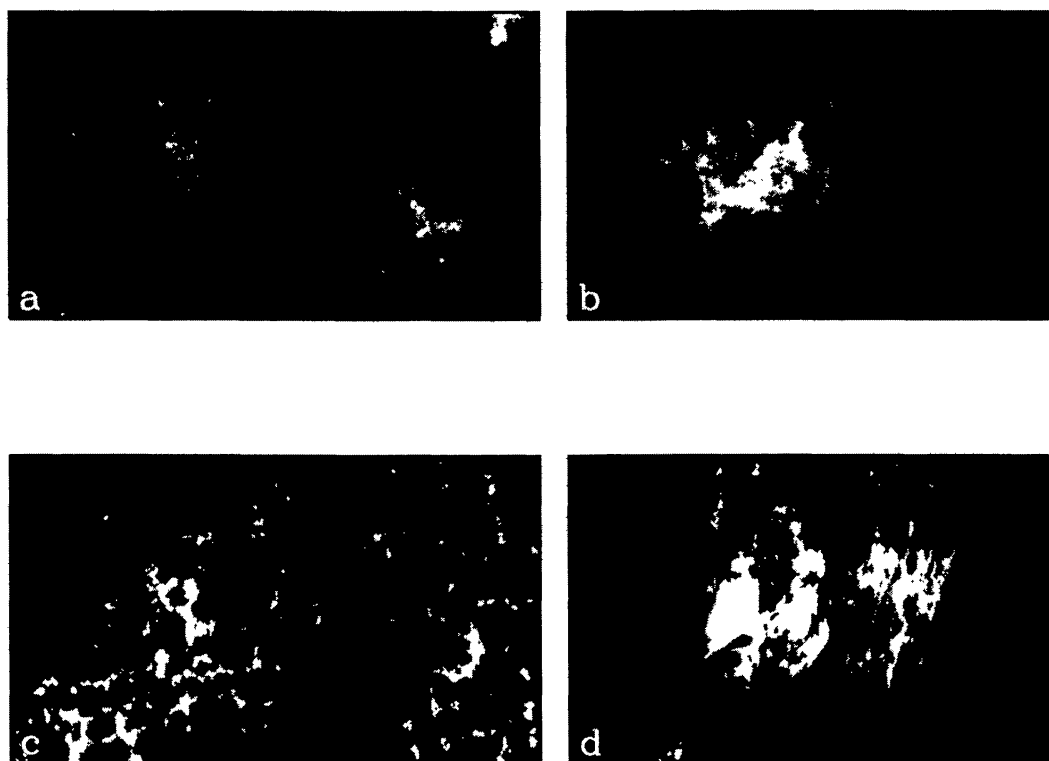


Fig. 8. Comparison of the He II 304 Å images ((a) east lobe, (b) west lobe) to corresponding NSO (Kitt Peak) magnetograms (c) and (d). White represents outwardly directed magnetic field, and black represents inwardly directed magnetic field.

5. Discussion

5.1. CORRELATIONS IN THE He I AND He II IMAGES

The similarities and differences in He II emission and He I absorption evident in Figure 5 can be put on a quantitative basis by plotting the He II 304 Å intensity against the equivalent width in He I for the same pixel position. Such plots are shown in Figures 9(a) and 9(b) for the east and west SERTS lobes, respectively. These data were derived from the reconstructed He II images (see Section 3.2). To decrease the spread due simply to single pixel noise, the images used to generate these plots were pixel-averaged by a factor of 5 down to a resolution of 4.5 arc sec. In the east lobe plot, filaments appear as an excess of population in the lower left. The active region appears as a population tail reaching to the right in the west lobe plot. The population reaching toward the top in the west lobe plot is an artifact of the pixels off the limb.

Upon examination of the scatter plots of He II emission versus He I absorption (represented by contour levels in Figure 9), and after some experimentation, it was decided that the quadratic polynomial given by the equation

$$y = 23.8 + (0.0168)x = (6.13 \times 10^{-7})x^2 \quad (1)$$

well represented the average behavior between the two species, where x is the He II

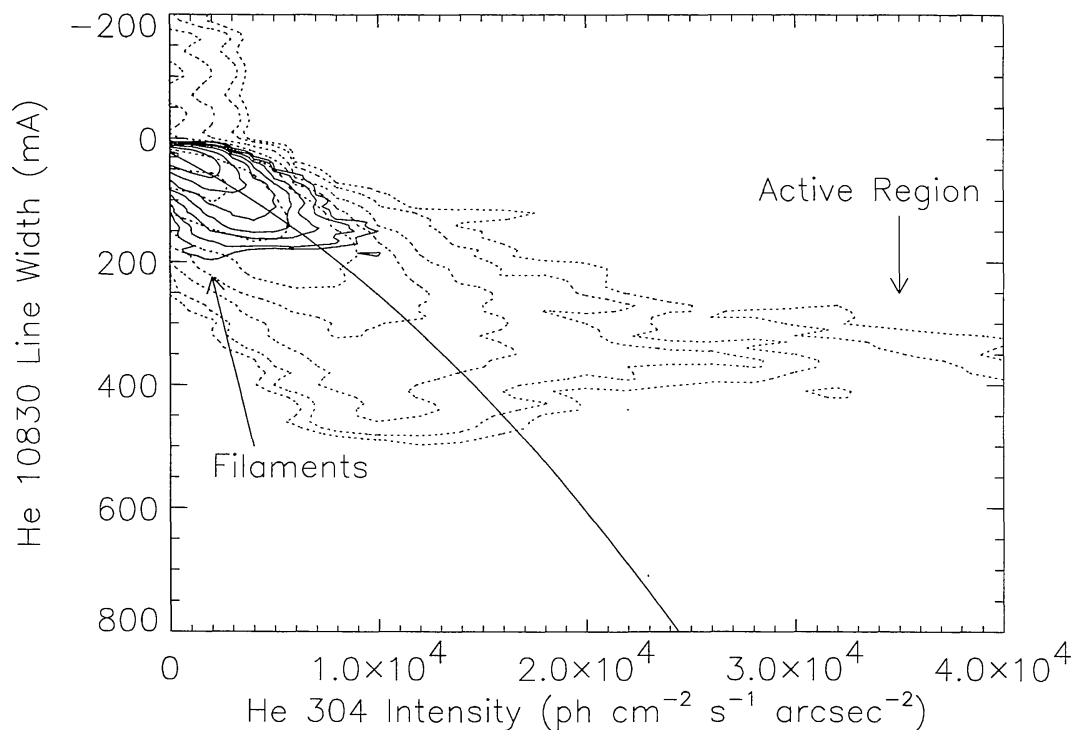


Fig. 9. Histogram map of He II 304 Å intensity versus He I 10830 Å equivalent line width. The solid contours are from the east lobe (quiet Sun) and the dashed contours are from the west lobe (active region). The contour levels shown are chosen from a logarithmic scale. The solid curve in both plots represents a least-squares fit of a quadratic polynomial to the data points. It is the difference between the He I 10830 Å values and this curve that is displayed as the difference images in Figure 10. The He II data are based on the reconstructed images (see Figure 4).

304 Å intensity in units of photons $\text{cm}^{-2} \text{s}^{-1} \text{arcsec}^{-2}$, and y is the He I 10830 Å equivalent line width in units of mÅ. However, no statistical significance should be applied to this equation, since the functional form is arbitrary, and the fit could only be achieved by rejecting points that appeared to be outside the main population of points. The fit was applied to the points from the east lobe (quiet Sun), and then compared to the data from the west lobe (which included the active region) where it also seemed to match the average behavior as well as could be determined.

It is possible to use Equation (1) and the He II 304 Å intensity values to predict what the corresponding He I 10830 Å equivalent line width should be if the correspondence were exact. Figure 10 shows the difference images of the true He I images and the images predicted in this manner. Filaments appear dark in both He I and He II (although less so in He II), and therefore appear as dark structures in the difference images. The bright active region emission surrounding the sunspot in He II is largely uncorrelated with the He I absorption, and therefore appears bright. The supergranulation network appears with more contrast in He I than in He II – a good example of this is the circled structure in the upper left-hand corner of the

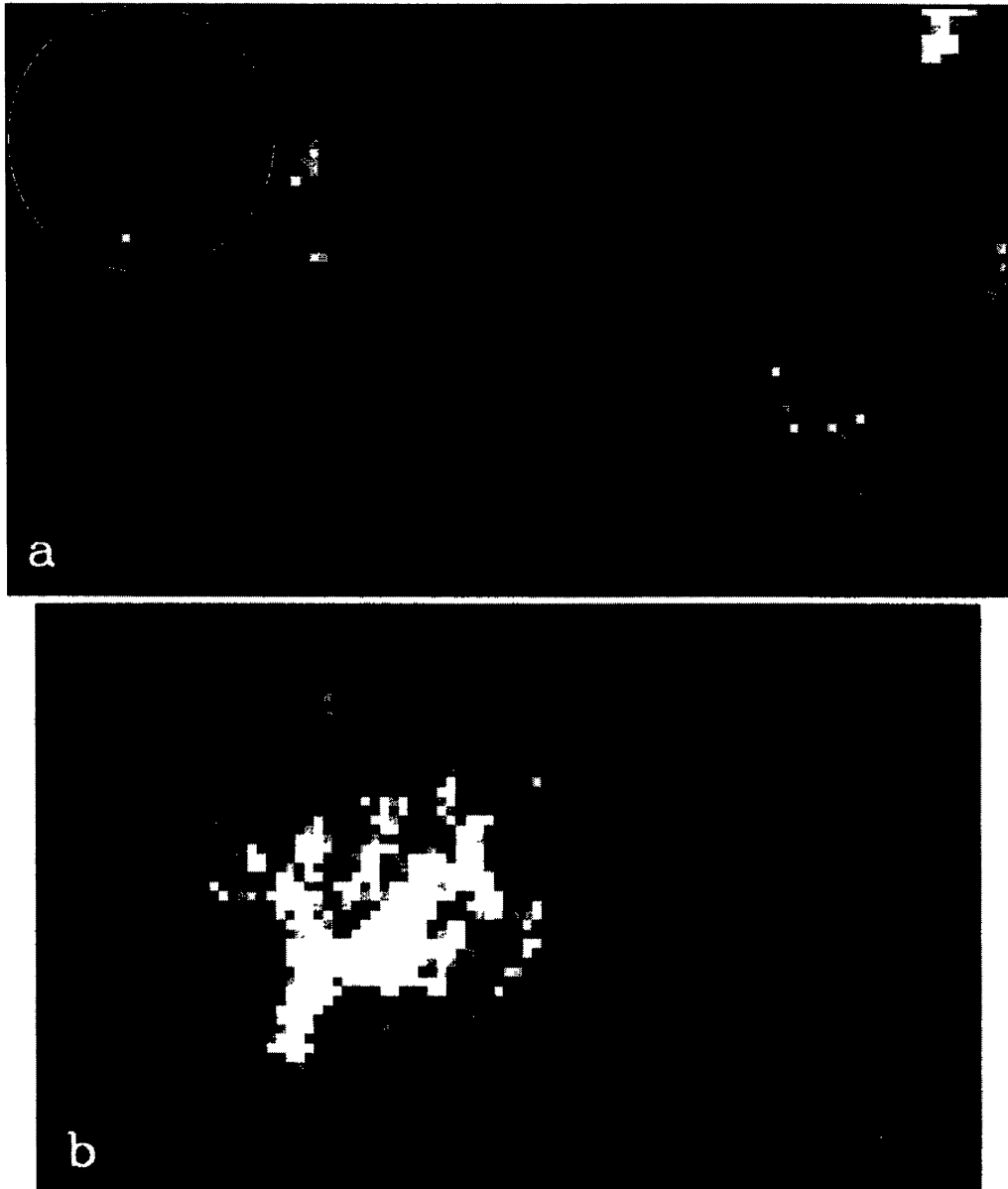


Fig. 10. Images ((a) east lobe, (b) west lobe) formed from the differences between the measured He I images and the predictions based on the reconstructed He II images (see Figures 5 and 9). In these images resolution has been degraded to 4.5 arc sec. Black pixels represent points where the He I image is darker than predicted, and white pixels are points that are less dark than predicted. The circle indicates an area where supergranulation is apparent.

east lobe. The fact that these images, which are essentially the residuals from the prediction given by Equation (1), exhibit structure shows that a large part of the scatter in Figure 9 does not arise from measurement error.

It is interesting to compare these results for the relationship between 304 Å emission and 10830 Å absorption with the earlier Skylab results reported by Harvey and Sheeley (1977). They too conclude that filaments exhibit strong absorption in 10830 Å and weak emission in 304 Å, and that the chromospheric network exhibits much greater contrast in 10830 Å than in 304 Å. They also note that limb-darkening

is clearly visible in the 10830 Å image, but only weakly so in the 304 Å image. In the dataset presented here, the 10830 Å exhibits no limb-darkening since it is presented as an equivalent line width, so we cannot comment on this effect, but the 304 Å data shows some darkening toward the limb (Figure 5(b)). In addition, we observe the same general correlation between strong coronal EUV emission and 10830 Å absorption that is reported for Skylab soft X-ray emission and 10830 Å absorption in Harvey *et al.* (1974, 1975). This can be seen by comparing Figures 2 and 3.

The effect of the image deconvolution process on the quantitative results from the SERTS images is hard to judge. Certainly, the form of the relationship between the He II 304 Å and He I 10830 Å lines (Figure 9) changes. We had expected that the scatter plot between the two lines would show a tighter relationship after deconvolution than before; this did not happen. A positive indication that the deconvolved intensities are more reliable than the raw measured values is that the match between the He I/He II relationship in the two lobes studied was closer after deconvolution than before. Also some distinction in the relationship we thought we saw before deconvolution were less clear after deconvolution, implying that those distinctions may have been artifact of the telescope resolution. For these reasons, only the comparison of the reconstructed He II data to the He I data is presented in Figures 9 and 10.

The coregistered images in 10830 Å, 304 Å, and a number of strong coronal lines, along with slit spectra in 304 Å and the same coronal lines, should permit an estimate to be made of the mechanism that populates the triplet ground-state of the 10830 Å line, whether primarily coronal radiation, 304 Å radiation, or local electron collisions, though an approximate treatment of the role of hydrogen L α will be needed in the analysis. This computation requires an estimation of the total coronal flux shortward of the head of the ionization limit of neutral He at 504 Å. Our observations cover only a portion of this spectrum, but an approximate method for estimating the total flux has been developed in a parallel study by Jordan *et al.* (1993) to explore the relative roles of local collisions and coronal radiation short of 228 Å in producing the upper level of the 304 Å line using these same SERTS-3 data.

6. Conclusions

The image reconstruction techniques used were quite successful at recovering the light spread out into the broad wings of the point-spread function, where most of the energy was, but did not sharpen the central core. The Richardson–Lucy technique was somewhat more successful than Fourier deconvolution in maintaining the sharpness of small features.

We have noted that these SERTS images may contribute to understanding the mechanisms controlling He I and He II line formation on the Sun. Specifically, they can be used to estimate the relative contribution of coronal radiation to producing

the He II 304 Å line, and the contributions of He II 304 Å emission and coronal radiation in producing the ground state of He I 10830 Å.

We have been able to confirm many of the conclusions of Harvey and Sheeley (1977) from their Skylab observation, namely:

- The He II emission and the He I 10830 Å absorption features are very highly correlated with each other.
- The supergranular network appears in greater contrast in 10830 Å than it does in 304 Å.
- Filaments appear much darker in 10830 Å than they do in 304 Å.

A significant difference between our observations and those of Harvey and Sheeley is that ours can be placed on a quantitative basis. Technical difficulties during the Skylab observation precluded obtaining quantitative results for the 10830 Å exposure.

The correlation between the He II 304 Å and He I 10830 Å lines seems to break down in the brightest plage areas in the active region around the sunspot. Although the He II line seems to follow the behavior of the chromospheric H α and Ca II 8542 Å lines, the He I line does not show such strong features. Neither are they seen in the coronal lines, although there is general correlation between the coronal radiation and the He II 304 Å emission and He I 10830 Å absorption.

Acknowledgements

The authors wish to thank H. Zirin of Big Bear Observatory for the H α full-disk image shown in Figure 1, and A. Poland for his comments on the draft of this paper. NSO/Kitt Peak data used here are produced cooperatively by NSF/NOAO, NASA/GSFC, and NOAA/SEL. This work was supported under NASA RTOP 879–11–38.

References

- Anderson, L. S. and Athay, R. G.: 1989, *Astrophys. J.* **336**, 1089.
- Avrett, E. H.: 1985, in B. W. Lites (ed.), *Chromospheric Diagnostics and Modelling*, Sunspot, NSO, p. 67.
- Brault, J. W. and White, O. R.: 1971, *Astron. Astrophys.* **13**, 169.
- Cook, J. W., Ewing, J. A., and Sutton, C. S.: 1988, *Publ. Astron. Soc. Pacific* **100**, 402.
- Davila, J. M., Thomas, R. J., Thompson, W. T., Keski-Kuha, R. A. M., and Neupert, W. M.: 1992, in *Proceedings 10th Colloquium on UV and X-ray Spectroscopy*, Berkeley, CA (in press).
- Harvey, J. W. and Sheeley, N. R.: 1977, *Solar Phys.* **54**, 343.
- Harvey, J. W., Krieger, A. S., Timothy, A. F., and Vaiana, G. S.: 1974, *Oss. Mem. Oss. Arcetri* **104**, 50.
- Harvey, J. W., Krieger, A. S., Davis, J. M., Timothy, A. F., and Vaiana, G. S.: 1975, *Bull. Am. Astron. Soc.* **7**, 358.
- Jones, H. P., Duvall, T. L. J., Harvey, J. W., Mahaffey, C. T., Schwitters, J. D., and Simmons, J. E.: 1992, *Solar Phys.* **139**, 211.
- Jordan, S. D., Thompson, W. T., Thomas, R. J., and Neupert, W. M.: 1993, *Astrophys. J.* (in press).
- Lehmann, H. and Häupl, W.: 1986, *AAS Photo-Bulletin* **43**, 5.

- Leviton, D. B., Wright, G. A., Thomas, R. J., Davila, J. M., and Epstein, G. L.: 1993, *Applied Optics* (in prep.).
- Lucy, L.: 1974, *Astron. J.* **79**, 745.
- Mein, N. and Mein, P.: 1977, *Solar Phys.* **49**, 231.
- Neupert, W. M., Brosius, J. W., Thomas, R. J., and Thompson, W. T.: 1992a, *Astrophys J.* **392**, L95.
- Neupert, W. M., Epstein, G. L., Thomas, R. J., and Thompson, W. T.: 1992b, *Solar Phys.* **137**, 87.
- Thomas, R. J. and Neupert, W. M.: 1993, *Astrophys. J.* (in prep.).
- Tsubaki, T. and Engvold, O.: 1975, *AAS Photo-Bulletin* **9**, 17.